Numerical and experimental study of the dynamics of a s helium plasma gun discharge with various amounts of N_2 admixture

2016 Plasma Sources Sci. Technol. 25 035002

(http://iopscience.iop.org/0963-0252/25/3/035002)

IOP Publishing Plasma Sources Science and Technology

Plasma Sources Sci. Technol. **25** (2016) 035002 (17pp) doi:10.1088/0963-0252/25/3/035002

Numerical and experimental study of the dynamics of a μs helium plasma gun discharge with various amounts of N_2 admixture

Anne Bourdon[1], Thibault Darny[2], François Pechereau[3], Jean-Michel Pouvesle[2], Pedro Viegas[1], Sylvain Iséni[2] and Eric Robert[2]

[1] LPP, UMR 7648, Ecole Polytechnique, route de Saclay, 91128 Palaiseau Cedex, France
[2] GREMI, UMR 7344 CNRS, Université d'Orléans, 45067 Orléans, France
[3] CERFACS, 42 Avenue Coriolis, 31057 Toulouse, France

E-mail: anne.bourdon@lpp.polytechnique.fr, jean-michel.pouvesle@univ-orleans.fr and eric.robert@univ-orleans.fr

Received 2 November 2015, revised 4 February 2016
Accepted for publication 10 February 2016
Published 23 March 2016

Abstract

This paper presents a combined 2D numerical and experimental study of the influence of N_2 admixture on the dynamics of a He–N_2 discharge in the 10 cm long dielectric tube of a plasma gun set-up. First, the comparison between experiments and simulations is carried out on the ionization front propagation velocity in the tube. The importance of taking into account a detailed kinetic scheme for the He–N_2 mixture in the simulations to obtain a good agreement with the experiments is put forward. For the μs driven plasma gun, the two- and three-body Penning reactions occurring in the plasma column behind the ionization front, are shown to play a key role on the discharge dynamics. In the experiments and simulations, the significant influence of the amplitude of the applied voltage on the ionization front propagation velocity is observed. As the amount of N_2 varies, simulation results show that the ionization front velocity, depends on a complex coupling between the kinetics of the discharge, the photoionization and the 2D structure of the discharge in the tube. Finally, the time evolution of axial and radial components of the electric field measured by an electro-optic probe set outside the tube are compared with simulation results. A good agreement is obtained on both components of the electric field. In the tube, simulations show that the magnitude of the axial electric field on the discharge axis depends weakly on the amount of N_2 conversely to the magnitude of the off-axis peak electric field. Both, simulations and first measurements in the tube or within the plasma plume show peak electric fields of the order of 45 kV·cm^{-1}.

Keywords: non-thermal atmospheric pressure plasma, plasma jets, plasma medicine, reaction kinetics, electric field, fluid simulation

(Some figures may appear in colour only in the online journal)

1. Introduction

Among the large variety of plasma jets (Lu *et al* 2012, Winter *et al* 2015a) developed for biomedical applications (Fridman *et al* 2008, von Woedtke *et al* 2013), the plasma gun (PG) has been shown to allow for the long distance delivery of plasmas through high aspect ratio dielectric capillaries and more recently across multi hole dielectric and metallic assemblies (Robert *et al* 2015). Although prior studies have dealt with the investigation of the plasma propagation modes in such

devices (Robert *et al* 2012), detailed propagation mechanisms still require dedicated analysis. As reported in Robert *et al* (2013), the application of PG in anti-tumor experiments and plasma delivery in endoscopic protocols are of great interest and represent an excellent opportunity for the development and optimization of new modes of operation of such system.

Recently, to tailor the generation of reactive species in plasma jets for biomedical applications, several research groups (e.g. Darny *et al* (2014), Iseni *et al* (2014), Reuter *et al* (2012) and van Gessel *et al* (2013)) have studied the use of gas admixtures. In particular, in Darny *et al* (2014), a nitrogen or oxygen admixture has been added in the helium buffer at the inlet of the PG hollowed electrode but also alternatively downstream along the helium plasma propagation inside long dielectric capillaries to change the plasma jet properties. Furthermore, there exists also a recent interest for the consideration of electric field associated with the plasma plume delivery over tissues in comparison with the previously reported potent effects of the pulsed electric fields (Zhang *et al* 2014).

To better understand and suggest future optimization pathways of plasma jets, tremendous experimental investigations are necessary to measure the many quantities (i.e. the ionization degree, electric field and species densities) which are for some of them difficult to measure accurately. Currently, a lot of effort has been made in that direction by different research groups (van Gessel *et al* 2013, Hübner *et al* 2014, Iseni *et al* 2014, Sretenović *et al* 2014, Winter *et al* 2015b). Another approach, used in this work, is to combine an experimental and a 2D modeling approach, as in Xiong *et al* (2012) and Xiong *et al* (2013), in order to have access to plasma features which are still challenging to measure. In particular, in this work, we study in detail the influence of N_2 admixture on the dynamics and structure of a He–N_2 discharge in the 10 cm long dielectric tube of a PG set-up.

In section 2, we present the experimental set-up and experimental results obtained in the basic PG configuration and in the modified PG set-up designed for comparison with simulations. In section 3, we set out the 2D fluid model used to simulate the discharge in the 10 cm long dielectric tube. Then, in section 4.1, simulation results obtained on the discharge dynamics and structure for the reference case with 1000 ppm of N_2 are presented and the numerical ionization front propagation velocity is compared with experiments. In section 4.2, an analysis of the importance of different reactions in the kinetic scheme of the He–N_2 mixture is carried out in simulations. Then in section 4.3, a comparison of the experimental and numerical results on the propagation velocity of the ionization front for various amounts of N_2 is presented. Finally, in section 4.4, the experimental and numerical time evolutions of the axial and radial electric fields are compared.

2. Experimental set-up and first experimental results

The basic PG configuration has been described in detail in Robert *et al* (2012). Briefly it consists in a dielectric barrier discharge reactor equipped with an inner hollowed electrode. The helium gas with varying admixtures is injected through the electrode and flows into the capillary tube. The inner electrode is powered with a microsecond high voltage power supply. The pulse shape is identical from pulse-to-pulse for different voltage amplitudes up to 20 kV, with both polarities and frequencies ranging from a few tens of Hz up to several kHz. The DBD reactor, namely the 4 mm inner diameter glass or quartz capillary is 1 mm thick and is equipped with an outer grounded ring electrode aligned with the inner electrode tip. Plasma ignition occurs across the two electrodes and then plasma propagation occurs in both the upstream and downstream directions. The downstream plasma propagation consists in the generation of so called pulsed atmospheric plasma streams (PAPS). The latter is the combination of an ionization front, revealed by intense light emission and strong axial electric field (Robert *et al* 2015) followed by a plasma tail connecting the ionization front with the powered electrode through a more or less resistive plasma column (Shashurin *et al* 2009, 2012, Xiong and Kushner 2012, Boselli *et al* 2015). In this work, the admixture of nitrogen in the buffer helium gas flow is controlled at the inlet of the PG DBD reactor with the use of mass flow controllers (Brooks). Besides the strong modification of plasma emission spectra associated with both direct electron impact on nitrogen molecules but also kinetic transfers from helium ionic and metastable states, drastic modulation of both the plasma stream propagation length and velocity occur. Figure 1 shows two photographs of the plasma generation inside a 40 cm long quartz capillary when the PG is flushed with either only helium at a flow rate of 1000 sccm or when an additional 1 sccm nitrogen flow rate is added while all other operation parameters of the plasma devices are identical (16 kV peak voltage amplitude, 1 kHz repetition rate). While with only the helium buffer, the PAPS remains confined in the dielectric capillary and reaches a length of propagation

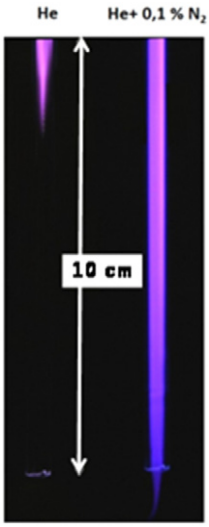

Figure 1. Photographs of PAPS (exposure time of 1 s) in the last 10 cm of a 40 cm long capillary. Left: emission of a helium-fed plasma gun. Right: He–N_2 mixture (1000/1 sccm) plasma emission. The bottom of the white arrow coincides with the capillary outlet.

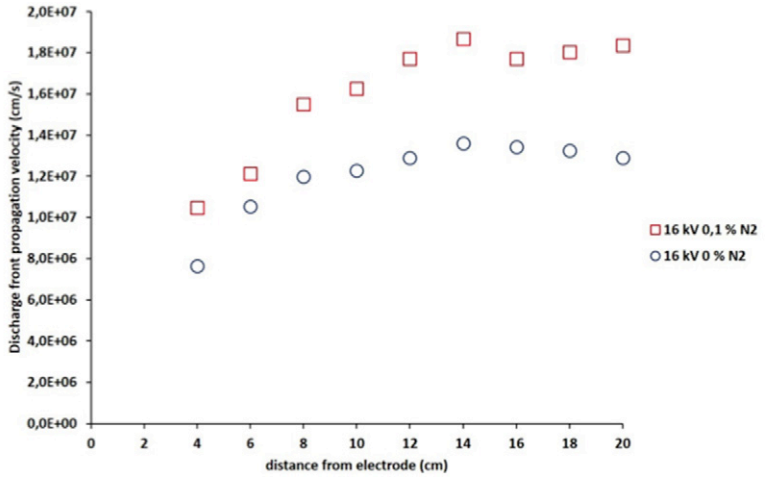

Figure 2. Evolution of the ionization front velocity versus the distance from the inner electrode tip for helium fed (circles) and He–N_2 mixture with 1000/1 sccm (squares) in the basic PG set-up.

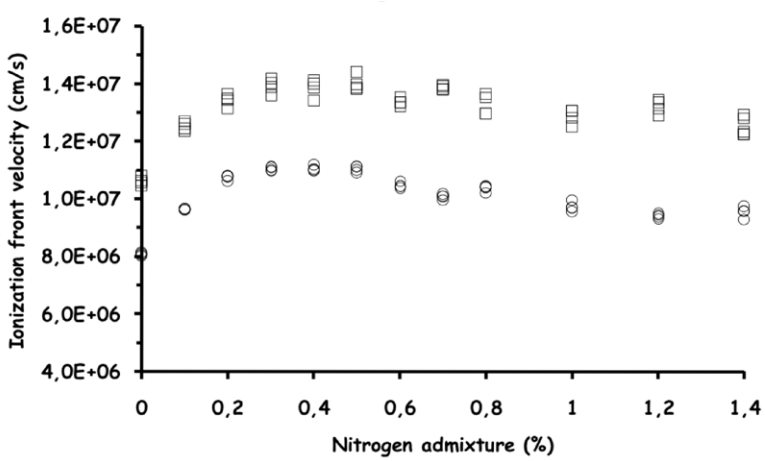

Figure 3. Evolution of the mean ionization front velocity over the first 8 cm of the PAPS propagation path versus the nitrogen admixture for 10 kV (circles) and 16 kV (squares) voltage peak amplitudes in the basic PG set-up.

slightly higher than 30 cm, the small nitrogen admixture results in the lengthening of the plasma streams over 10 cm inside the capillary and leads to the generation of the plasma plume at the capillary outlet. At the same time, figure 2 reveals that the ionization front velocity is also significantly modified with such a minor nitrogen admixture. In figure 2, the ionization front velocity is measured with a 10 optical fiber bunch connected to a fast rise time photomultiplier tube (Hamamatsu R955). Each optical fiber inlet is set along a 20 cm long quartz capillary with a separation of 2 cm between successive fibers. For the helium fed PG, the velocity gradually increases along the first 10 cm downstream from the inner electrode tip and stabilizes to 1.2×10^7 cm·s^{-1} along the next 10 cm. This velocity profile is correlated with the microsecond voltage waveform applied across the PG electrodes. Plasma ignition occurs on the rising front (2 μs in duration) of the voltage waveform at the instant when the voltage amplitude is about 2 kV and then the plasma stream propagation occurs while the voltage gradually increases up to its peak value (16 kV in figure 2) reached 2 μs after the voltage pulse onset. As the plasma stream extends from the inner electrode tip, the plasma column impedance increases together with the voltage drop across this plasma tail connecting the powered electrode to the ionization front. The combination of the temporal profile of the voltage waveform and the plasma tail increasing impedance results in the stabilization of the ionization front velocity as shown in figure 2, while for longer propagation lengths the velocity will finally gradually decrease (not shown in figure 2). With 0.1% nitrogen admixture the plasma ignition delay is shortened, as will be documented in the next sections, and the plasma front velocity is significantly increased (by 40%) to get stabilized to about 1.8×10^7 cm·s^{-1} at distances ranging from 12 to 20 cm downstream of the powered electrode. In figure 3, the evolution of the mean ionization front velocity over the first 8 cm of the PAPS propagation path, is presented versus the nitrogen admixture for two (10 and 16 kV) peak voltage amplitudes. The velocity profiles versus nitrogen admixture are quite similar for the two voltage amplitudes, the ionization front velocity being significantly higher (about 40%) for the highest voltage. It is worthwhile noting that there exists an optimum nitrogen admixture range, 0.2 to 0.8% for 16 kV and 0.2 to 0.6% for 10 kV, for which the mean velocity reaches its maximum value along the first 8 cm of the PAPS propagation path.

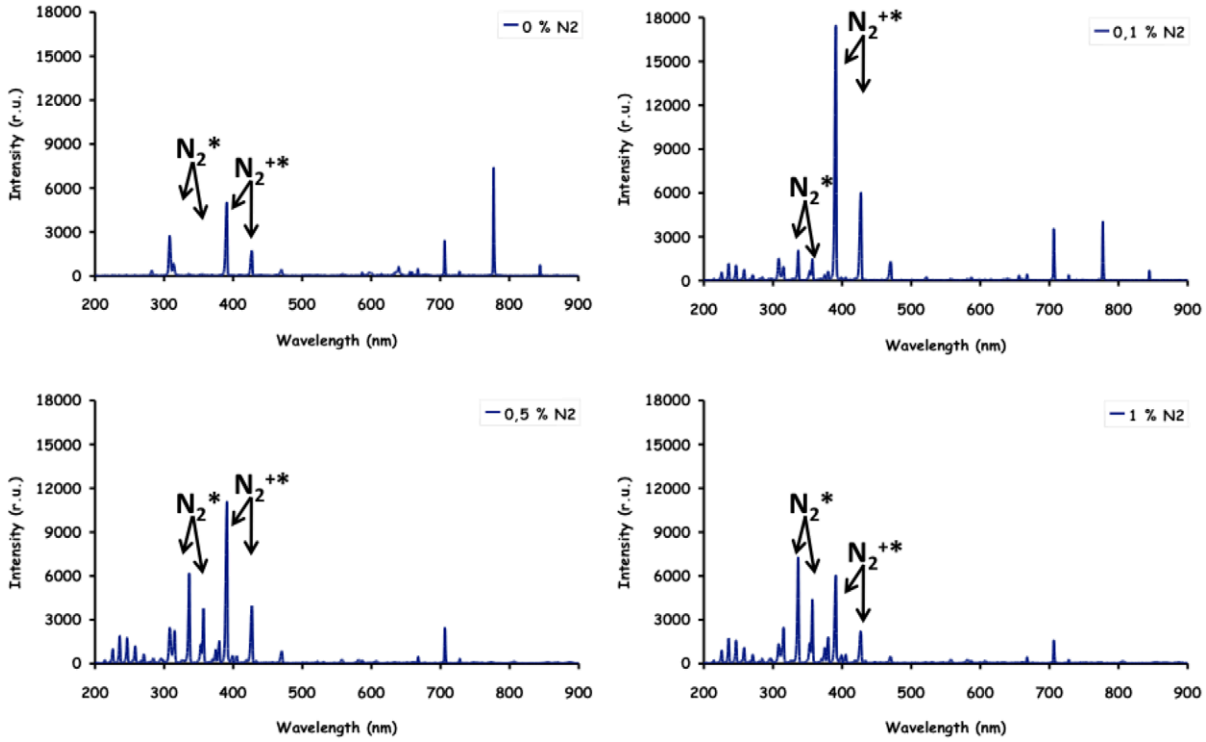

Figure 4. Time integrated optical emission spectra of the discharge for He (top left), and 0.1%, 0.5% and 1% N_2 admixtures. Spectra were collected 5 cm downstream the inner electrode tip in the basic PG set-up.

As already mentioned, the first interest of using nitrogen admixture for biomedical applications lies in the possibility to tailor the generation of reactive species. While the quantitative determination of many radical concentrations requires rather sophisticated diagnostics which was out of the scope of the present work, optical emission spectroscopy is a convenient tool (Gazeli *et al* 2012) to provide a first approach on the evolution of the plasma excitation mode with varying the operation parameters of the PG. This approach is also relevant for comparison with the kinetic scheme suggested in the modeling part of this work. Figure 4 presents four emission spectra collected with a compact UV-visible spectrometer (Maya Pro 2000) for helium fed (1000 sccm) and three nitrogen admixtures (0.1, 0.5 and 1%) flushed in the PG operated for the 16 kV peak voltage pulse delivered at 1 kHz repetition rate. Emission spectra in figure 4, clearly indicate that severe modulations of the excited levels of biologically active radicals (OH^* (282 and 308 nm), NO^* (200–300 nm), O^*(777 and 844 nm)) but also drastic modifications of the helium lines (e.g. 706 nm) and neutral (316, 337, 357, 380 nm) and ionic (391 and 428 nm) nitrogen bands are induced depending on the nitrogen admixture. Oxygen, nitrogen and hydroxyl radical excitation results from gas impurities and water vapor traces inside the capillary. For a helium-fed PG, the strongest emissions are OH^* and O^* while N_2^* are hardly excited and NO^* bands were not detected. For 0.1 and 0.5% nitrogen admixtures, the strongest bands turn to be N_2^{+*}, while O^* gradually vanishes and both N_2^* and NO^* bands continuously increase. For the highest nitrogen content (1%), N_2^* bands become the strongest emission. Both OH^* and He^* emission appear to be the less sensitive to the nitrogen admixture, exhibiting only small modulation of their intensity over the range of investigation. It is interesting to note that the highest ionization front velocity in figure 3 in the range of 0.2 to 0.8% nitrogen admixture, coincides with the highest production of the N_2^{+*} bands in the He–N_2 Penning mixture. For higher N_2 amounts, electron impact excitation of the N_2 second positive system becomes predominant and reveals a presumably lower electron temperature of the plasma.

In this work, to compare with simulations, a modified PG configuration was developed with a single high voltage ring electrode set around the quartz capillary. The whole set-up was set at the center of a 20 cm in diameter grounded cylinder. Minor modifications of the ignition voltage and timing, documented in the next sections, have been measured in comparison with those associated with the basic PG configuration. The key impacts of nitrogen admixtures on the plasma front velocity, plasma propagation length and optical emission were measured with about the same amplitudes and over the same range of investigated parameters for both the modified and basic PG set-ups. In the modified PG set-up, the ionization front velocity is measured with 3 optical fibers. The first fiber inlet is set at 2 cm from the high voltage ring. The following fibers are located at 3 cm from each other along the capillary tube. Figure 5 shows the evolution of the mean ionization front velocity along the first 8 cm of the PAPS propagation path versus the nitrogen admixture for two (10 kV and 16 kV) voltage peak amplitudes with the modified PG set-up. As previously discussed on figure 3, the velocity profiles versus N_2 admixture are quite similar for the two voltage amplitudes, the ionization front velocity being significantly higher for the highest voltage. It is worthwhile noting that the optimum N_2

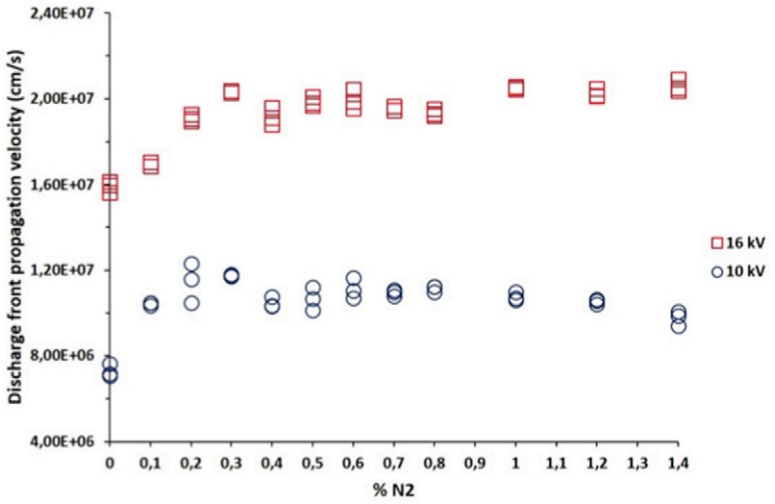

Figure 5. Evolution of the mean ionization front velocity over the first 8 cm of the PAPS propagation path versus the N_2 admixture for two 10 kV (circles) and 16 kV (squares) voltage peak amplitudes for the modified PG set-up.

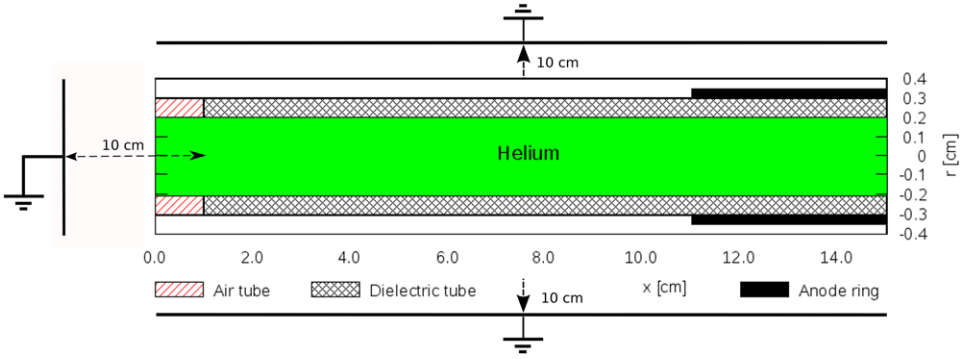

Figure 6. Side view schematics of the discharge set-up used in the simulations.

admixture range for which the mean velocity reaches its maximum value along the first 8 cm of the PAPS propagation path extends from 0.2 to 0.8% for 10 kV. For 16 kV, the maximum velocity is reached for N_2 admixtures higher than 0.2% as in the basic PG set-up, and is kept constant up to 1.4% of N_2 admixture.

Finally, an electro-optic sensor (eoSense Kapteos) equipped with an isotropic crystal probed by a laser beam was used to investigate the electric field strength. This sensor gives simultaneous access to two orthogonal components of the electric field (EF). In this work, a specially designed 1.75 mm in diameter, 1 mm long crystal embedded in an alumina tube, set at one end of an optical fiber was used as a sensor. The orientation between the capillary tube and the probe is a very sensitive parameter as two orthogonal EF components are measured. A preliminary experiment was performed in a dedicated plane-to-plane configuration. The resulting uniformly polarized EF was used to determine accurately the two axes of the probe and to calibrate the absolute EF strength. In this work, to compare with simulations, EF components were measured in a non intrusive, non perturbative way, 1 mm apart from the quartz capillary outer surface, i.e. at a mean radial position of 0.35 cm with respect to the capillary axis in the modified PG set-up. Then the EF sensor was moved with the use of a 2D translation stage equipped with two stepping motors. The experimental results as well as the comparison with simulation results are presented and discussed in section 4.4.

3. Numerical model

Numerical simulations have been carried out at atmospheric pressure and $T = 300$ K to comply with experiments. For comparison purposes, the geometries of the set-ups used for simulations and experiments are as close as possible. In particular, as shown on figure 6, the discharge set-up is placed in a grounded cylinder with a radius of 10 cm and a grounded plane is set at 10 cm of the dielectric tube exit. As in the experiments a quartz tube is used, in simulations, a dielectric tube with a relative permittivity of $\varepsilon_r = 4$ is considered. In this work, we focus on the dynamics of the discharge in the dielectric tube and then the influence of the helium-air mixing at the tube exit is neglected. In the simulations, as shown on figure 6, a volume filled with static helium is considered with a small and uniform admixture of N_2. In experiments, the helium flow velocity is slightly higher than 1 m·s^{-1} while the PAPS velocity is in the range of 10^5 m·s^{-1}, so the hypothesis of static helium is relevant during the few microseconds simulated during which the gas flow is frozen and no species diffusion has to be considered. In the simulations, the amount of N_2 admixture is varied from 10 to 10 000 ppm (where 1000 ppm

Table 1. List of chemical reactions.

Nos	Reaction	Rate coefficient	Reference
R1	$He + e^- \rightarrow He^+ + 2e^-$	$f(E/N)$	Hagelaar and Pitchford (2005)
R2	$N_2 + e^- \rightarrow N_2^+ + 2e^-$	$f(E/N)$	Hagelaar and Pitchford (2005)
R3	$He + e^- \rightarrow He^* + e^-$	$f(E/N)$	Hagelaar and Pitchford (2005)
R4	$N_2 + e^- \rightarrow N_2(C^3\Pi_u) + e^-$	$f(E/N)$	Hagelaar and Pitchford (2005)
R5	$N_2 + e^- \rightarrow N_2^+(B) + 2e^-$	$f(E/N)$	Hagelaar and Pitchford (2005)
R6	$He^* + e^- \rightarrow He + e^-$	2.9×10^{-9} cm^3 s^{-1}	Pouvesle *et al* (1982)
R7	$He^* + He^* \rightarrow He^+ + He + e^-$	4.35×10^{-10} cm^3 s^{-1}	Pouvesle *et al* (1982)
R8	$He^* + He^* \rightarrow He_2^+ + e^-$	1.015×10^{-9} cm^3 s^{-1}	Pouvesle *et al* (1982)
R9	$He^* + N_2 \rightarrow He + N_2^+ + e^-$	3.8×10^{-11} cm^3 s^{-1}	Pouvesle *et al* (1982)
R10	$He^* + N_2 + He \rightarrow 2He + N_2^+ + e^-$	1.65×10^{-30} cm^6 s^{-1}	Pouvesle *et al* (1982)
R11	$He_2^+ + e^- \rightarrow He + He$	4.0×10^{-9} cm^3 s^{-1}	Pouvesle *et al* (1982)
R12	$N_2^+ + e^- \rightarrow N + N$	1.0×10^{-7} cm^3 s^{-1}	Pouvesle *et al* (1982)
R13	$He^+ + 2He \rightarrow He_2^+ + He$	1.5×10^{-31} cm^6 s^{-1}	Pouvesle *et al* (1982)
R14	$He_2^+ + N_2 \rightarrow N_2^+ + 2He$	0.275×10^{-9} cm^3 s^{-1}	Pouvesle *et al* (1982)
R15	$He_2^+ + N_2 + He \rightarrow N_2^+ + 3He$	0.34×10^{-29} cm^6 s^{-1}	Pouvesle *et al* (1982)
R16	$He_2^+ + e^- \rightarrow He^* + He$	5.0×10^{-9} cm^3 s^{-1}	Pouvesle *et al* (1982)
R17	$He^* + 2He \rightarrow He_2^* + He$	1.9×10^{-34} cm^6 s^{-1}	Pouvesle *et al* (1982)
R18	$He^+ + N_2 \rightarrow He + N_2^+$	1.2×10^{-9} cm^3 s^{-1}	Pouvesle *et al* (1982)
R19	$He^+ + N_2 + He \rightarrow 2He + N_2^+$	2.2×10^{-29} cm^6 s^{-1}	Pouvesle *et al* (1982)
R20	$He^* + N_2 \rightarrow He + N_2^+(B) + e^-$	3.8×10^{-11} cm^3 s^{-1}	Pouvesle *et al* (1982)
R21	$He^* + N_2 + He \rightarrow 2He + N_2^+(B) + e^-$	1.65×10^{-30} cm^6 s^{-1}	Pouvesle *et al* (1982)
R22	$N_2^+(B) + e^- \rightarrow N + N$	1.0×10^{-7} cm^3 s^{-1}	Pouvesle *et al* (1982)
R23	$He_2^+ + N_2 \rightarrow N_2^+(B) + 2He$	0.825×10^{-9} cm^3 s^{-1}	Pouvesle *et al* (1982)
R24	$He_2^+ + N_2 + He \rightarrow N_2^+(B) + 3He$	1.02×10^{-29} cm^6 s^{-1}	Pouvesle *et al* (1982)
R25	$N_2^+(B) \rightarrow N_2^+ + h\nu$	1.5×10^7 s^{-1}	Pouvesle *et al* (1982)
R26	$N_2(C^3\Pi_u) + N_2 \rightarrow$ products	8.0×10^{-11} cm^3 s^{-1}	Naidis (2011b)
R27	$N_2(C^3\Pi_u) + He \rightarrow$ products	1.0×10^{-12} cm^3 s^{-1}	Naidis (2011b)
R28	$N_2(C^3\Pi_u) \rightarrow N_2(B^3\Pi_g) + h\nu$	2.4×10^7 s^{-1}	Naidis (2011b)
R29	$N_2^+ + 2N_2 \rightarrow N_4^+ + N_2$	5×10^{-29} cm^6 s^{-1}	Kossyi *et al* (1992)
R30	$N_4^+ + e^- \rightarrow N_2 + N_2$	2×10^{-6} cm^3 s^{-1}	see text
R31	$N_4^+ + N_2 \rightarrow N_2^+ + 2N_2$	2.5×10^{-15} cm^3 s^{-1}	Kossyi *et al* (1992)

Note: For simplicity, He(2^3S) is noted He*.

of N_2 corresponds to $X_{N_2} = N_{N_2}/N = 10^{-3} = 0.1\%$, with $N = 2.45 \times 10^{19}$ cm^{-3}, the neutral gas density at $T = 300$ K). As ionization in air is more difficult than in helium, air at the tube exit and around the dielectric tube is modeled as a dielectrics with a permittivity $\varepsilon_r = 1$. To compare with experiments, the same applied voltage waveforms are used with a 2 μs rise time and two peak voltages of 10 and 16 kV. In the following, the value of the peak voltage is referred to as the applied voltage.

In order to study the influence of different amounts of N_2 admixture on the helium discharge dynamics, a detailed kinetic scheme has to be used. However, it is important to note that so far, there is no reference kinetic scheme for He–N_2 atmospheric pressure plasma jets and different kinetic schemes have been used in the literature (Sommerer and Kushner 1992, Petrov *et al* 2000, Sakiyama and Graves 2006, Zhang and Kortshagen 2006, Martens *et al* 2008, Naidis 2011a, 2011b, Murakami *et al* 2013, Jánský and Bourdon 2014, Lazarou *et al* 2015, Lieberman 2015). Furthermore, as in this work a μs pulsed voltage source is used, it is important to take into account also in the kinetic scheme all recombination processes that may occur on μs timescales during the discharge propagation. As a reference, we have used the kinetic scheme derived in Pouvesle *et al* (1982) based on the detailed experimental study of an atmospheric pressure post-discharge in helium with 6 to 700 ppm of N_2. In table 1, it corresponds to reactions R6 to R25. It is interesting to note that in Pouvesle *et al* (1982), the only helium excited state is He(2^3S), which is denoted He* for simplicity in the following. In comparison to Pouvesle *et al* (1982), we have only neglected the influence of N(^{4}S) and N^+. Pouvesle *et al* (1982) have put forward the importance of taking into account three-body Penning (R10 and R21) and charge exchange (R15 and R24) reactions in atmospheric pressure helium discharges with N_2 admixtures. In the

Table 2. Additional reactions considered in section 4.2.

Nos	Reaction	Rate coefficient	Reference
R32	$N_2^+ + N_2 + He \rightarrow N_4^+ + He$	1.9×10^{-29} cm^6 s^{-1}	Martens *et al* (2008)
R33	$N_4^+ + He \rightarrow N_2^+ + N_2 + He$	2.5×10^{-15} cm^3 s^{-1}	Martens *et al* (2008)

following sections, the importance of these reactions on the discharge dynamics is studied. In table 1, we have added electron impact excitation and ionization reactions (reactions R1 to R5) and deexcitation reactions of $N_2(C^3\Pi_u)$ (R26 to R28) (Naidis 2011a, 2011b). In Pouvesle *et al* (1982), for helium discharges with 6 to 700 ppm of N_2, the only molecular ions are He_2^+, N_2^+ and $N_2^+(B)$. It is interesting to note that $N_2^+(B)$, which is a radiative state, can be used to monitor the time evolution of helium species if $N_2^+(B)$ is produced mainly by Penning (R20 and R21) and charge exchange (R23 and R24) reactions. As in this work, the amount of N_2 admixture is varied up to 10 000 ppm, we have also added reactions to take into account the kinetics of N_4^+ ions with charge exchange reactions (R29 and R31) and the dissociative recombination reaction of N_4^+ (R30). For the rate coefficient of R30, the upper limit of the value given by Kossyi *et al* (1992) is taken to comply with the constant value used in Pouvesle *et al* (1982) for the dissociative recombination reaction of N_2^+ (R12).

In the simulations of an atmospheric pressure dielectric barrier discharge in helium, Martens *et al* (2008) have shown that the major ion could be N_4^+ when the N_2 impurity level is higher than about 20 ppm. In their work, the production of N_4^+ is determined by the associative reaction of N_2^+ with N_2 and He as a third partner (R32 in table 2), the destruction of N_4^+ by the dissociative recombination (R30) and the dissociative collision with He (R33 in table 2). In section 4.2, the influence of the reactions of table 2 on the discharge dynamics in the dielectric tube will be discussed.

Finally, the chemical model used is this work takes into account 8 species (five positive ions: He^+, He_2^+, N_2^+, $N_2^+(B)$ and N_4^+, two excited species: He^* and $N_2(C^3\Pi_u)$ and electrons) and 31 reactions given in table 1. As in Jánský and Bourdon (2014), a classical fluid model based on continuity equations for electrons, ions and excited species coupled with Poisson's equation is used to simulate the discharge propagation in cylindrical coordinates (x, r). Surface charges on the dielectric surface are obtained by time integrating charged particle fluxes to the surface. At the dielectric surface, secondary emission of electrons by ion bombardment ($\gamma = 0.1$ for all ions) is taken into account. We have checked that the variation of the value of γ in the range 0.01 to 0.1 has a negligible influence on the discharge structure and dynamics described in this work. As in Jánský and Bourdon (2014), the local field approximation is used and it is assumed that electron transport parameters and reaction rates of electron impact excitation and ionization reactions (R1 to R5) are functions of the local reduced electric field E/N, where E is the magnitude of the electric field. These coefficients are taken from BOLSIG + (Hagelaar and Pitchford 2005) with the IST-Lisbon database (2014). In particular, we have noted that the amount of N_2 admixture has only a small influence of the electron mobility and electron diffusion coefficient for a N_2 admixture varying between 10 and 10 000 ppm. Positive ion mobilities are derived from Ellis *et al* (1976). For the simulations carried out in this work, the reduced electric field remains less than 200 Td. For this range, ion mobilities vary less than 50% and then we have considered constant average values for ion mobilities: $\mu_{He^+} = 10.0$, $\mu_{He_2^+} = 17.5$ and $\mu_{N_2^+} \approx \mu_{N_2^+(B)} \approx \mu_{N_4^+} = 20$ cm$^2 \cdot$(V $\cdot$ s)$^{-1}$. Diffusion coefficients for ions are evaluated using the Einstein relation with a gas temperature of $T = 300$ K.

In this work, for the photoionization model, we use a simple approach similar to the one proposed by Naidis (2010). We assume that the VUV radiation emitted by excited helium species is absorbed by nitrogen molecules of the admixture and ionizes them. As mentioned in Naidis (2010), at atmospheric pressure, the ionizing radiation is emitted mainly by the excited molecules He_2^* produced by the three-body conversion reaction R17 involving excited helium atoms. Then, as in Naidis (2010), the ionizing radiation is assumed to be proportional to the excitation rate S_{exc} of helium atoms by impact of electrons ($S_{exc} = n_e n_{He} k_{R_3}$ where n_e and n_{He} are the electron and helium densities and k_{R_3} is the rate coefficient of reaction R3 in table 1). The absorption coefficient of the ionizing radiation k_{ph} is assumed to depend on the level of nitrogen admixture as $k_{ph} = N X_{N_2} \sigma_{ph}$, where for the photoionization cross section a typical value of $\sigma_{ph} = 3 \times 10^{-17}$ cm^2 is assumed as in Naidis (2010). Then, the photoionization rate at point of observation $\mathbf{r}$ of the computational domain of volume V' due to source points emitting photons at $\mathbf{r}'$ can be written as:

$$S_{ph}(\mathbf{r}) = \xi X_{N_2} \iiint_{V'} S_{exc}(\mathbf{r}') \frac{\exp(-k_{ph}\mathbf{R})}{4\pi R^2} dV' \qquad (1)$$

where $R = |\mathbf{r} - \mathbf{r}'|$. As expected, the photoionization source term is proportional to the amount of N_2 admixture and in the following we use $A_{ph} = \xi X_{N_2}$. In Naidis (2010), the proportionality coefficient ξ is varied in the range 0.1–1 and was set equal to 1 in Jánský and Bourdon (2014). In this work, we have varied ξ over a wide range, and we present in section 4 the results obtained in the range 1–10, for which the best agreement with experiments has been obtained. For the calculation of the photoionization source term, the SP3 approximation of the radiative transfer equation (Bourdon *et al* 2007) with Larsen's boundary condition (Liu *et al* 2007) is used considering for the He–N_2 mixture only one absorption length.

The code used for this study is mainly the OPENMP-MPI parallelized version of the code used in Pechereau *et al* (2012). Two main differences have to be mentioned: first, to solve Poisson's equation and Poisson type equations for the photoionization source term we have implemented the iterative solver SMG in the (HYPRE 2007) library. Second, for the time integration of the detailed chemistry, we have used the implicit 5th order RADAU solver (Hairer and Wanner 1996). Other characteristics of the simulations (mesh used, boundary conditions, numerical methods and time-step calculation) are presented in detail in Pechereau (2013). The average

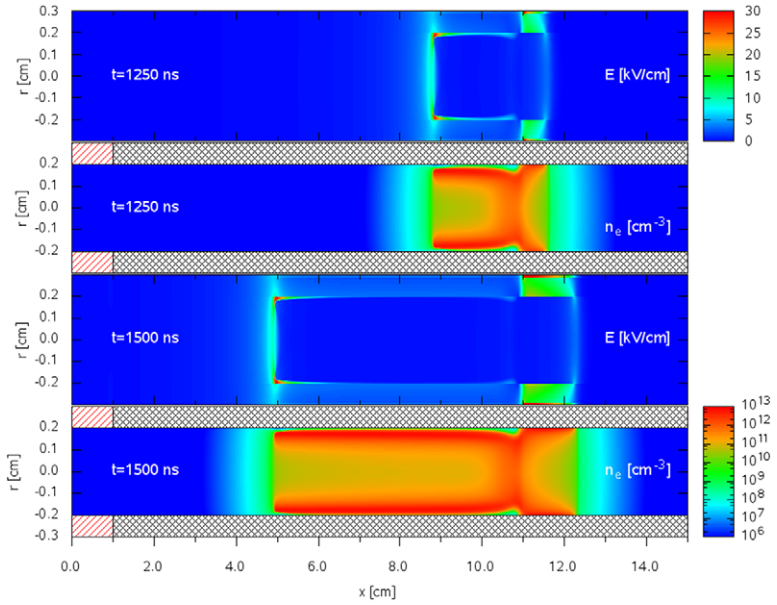

Figure 7. Cross-sectional views of the magnitude of the electric field and electron density at $t = 1250$ and 1500 ns for an applied voltage of 16 kV, 1000 ppm of N_2, with a preionization level $n_{init} = 10^4$ cm^{-3} and for a photoionization coefficient $A_{ph} = 10^{-2}$.

computational time of the simulation results presented in this paper are of one day with 4 MPI processes and 12 OPENMP threads on a multicore cluster (Altix ICE 8400 LX of 68 nodes with two processors six-core Intel Xeon X5650 per node and with 24 Go of memory per node) for a cartesian mesh with 7639×276 points.

With the low repetition frequency of the applied voltage used in experiments, as initial conditions, we have considered no initial surface charges on the inner dielectric tube surface and a uniform initial preionization density n_{init} of electrons and positive ions in the He–N_2 mixture in the tube. In this work, this uniform density is varied over several orders of magnitude to study its influence on the discharge dynamics. This will be discussed in section 4.1. Finally, to compare with experiments, we have computed the propagation velocity of the ionization front in the dielectric tube. For this, in each output file stored every 50 ns, the axial position of the peak electric field in the dielectric tube has been located. The propagation velocity of the ionization front is simply calculated based on the difference of axial positions of the peak electric field between two output files, divided by 50 ns.

4. Results

4.1. Discharge dynamics and structure for the reference case with 1000 ppm of N_2

In this section, we present simulation results on the dynamics of the discharge in the tube with, as a reference, 1000 ppm of N_2. Figure 7 shows the time sequence of the distributions of the electron density and absolute values of the electric field at $t = 1250$ and 1500 ns, for an applied voltage of 16 kV with an initial preionization level $n_{init} = 10^4$ cm^{-3} and for a photoionization coefficient $A_{ph} = 10X_{N_2} = 10^{-2}$. As already observed in previous experimental and numerical works as in Algwari and O'Connell (2011) and Jánský and Bourdon (2011), with a positive high voltage ring electrode around the dielectric tube, the discharge ignition occurs at the outer edge of the high-voltage electrode and two ionization fronts start propagating; one weak negative ionization front propagates mostly on the tube surface below the high voltage electrode and a positive ionization front propagates toward the tube exit. In the following, to compare with experiments, we focus on the dynamics and structure of the positive ionization front. For the conditions of figure 7, we observe a rapid and stable propagation of the positive ionization front in the 10 cm long tube. This positive ionization front has a tubular structure with peaks of electric field and electron density close to the inner dielectric tube surface. For the same conditions as figure 7, figure 8 shows at $t = 1500$ ns that the spatial distribution of all species are rather different. In particular, we note that He^+ and He^* are formed in the positive ionization front, by electron impact ionization and excitation of He. Whereas the He^* density remains high in the plasma column, we note that the He^+ ions are rapidly converted in He_2^+ and then in $N_2^+(B)$ and N_2^+. In the conditions of figure 7, N_2^+ is the major ion in the plasma column. With the chemical model of table 1, figure 8 shows that N_4^+ is only a minor ion in the plasma column for 1000 ppm of N_2.

As a first step in the comparison of experimental and numerical results, we compare in table 3 the measured and computed ignition times of the discharge in the tube for 1000 ppm of N_2 for the two applied voltages of 10 and 16 kV. Experimentally, the plasma ignition time τ_{igni}^{exp} is associated with the onset of light emission captured by an optical fiber positioned in the closest vicinity of the inner electrode tip. The experimental ignition times given in table 3 have been measured for a pulsed voltage with a repetition rate of 1 kHz. It is interesting to note that as part of preparatory work for the experimental results presented in this paper we have varied the repetition rate between 200 Hz and 2 kHz. Only a small

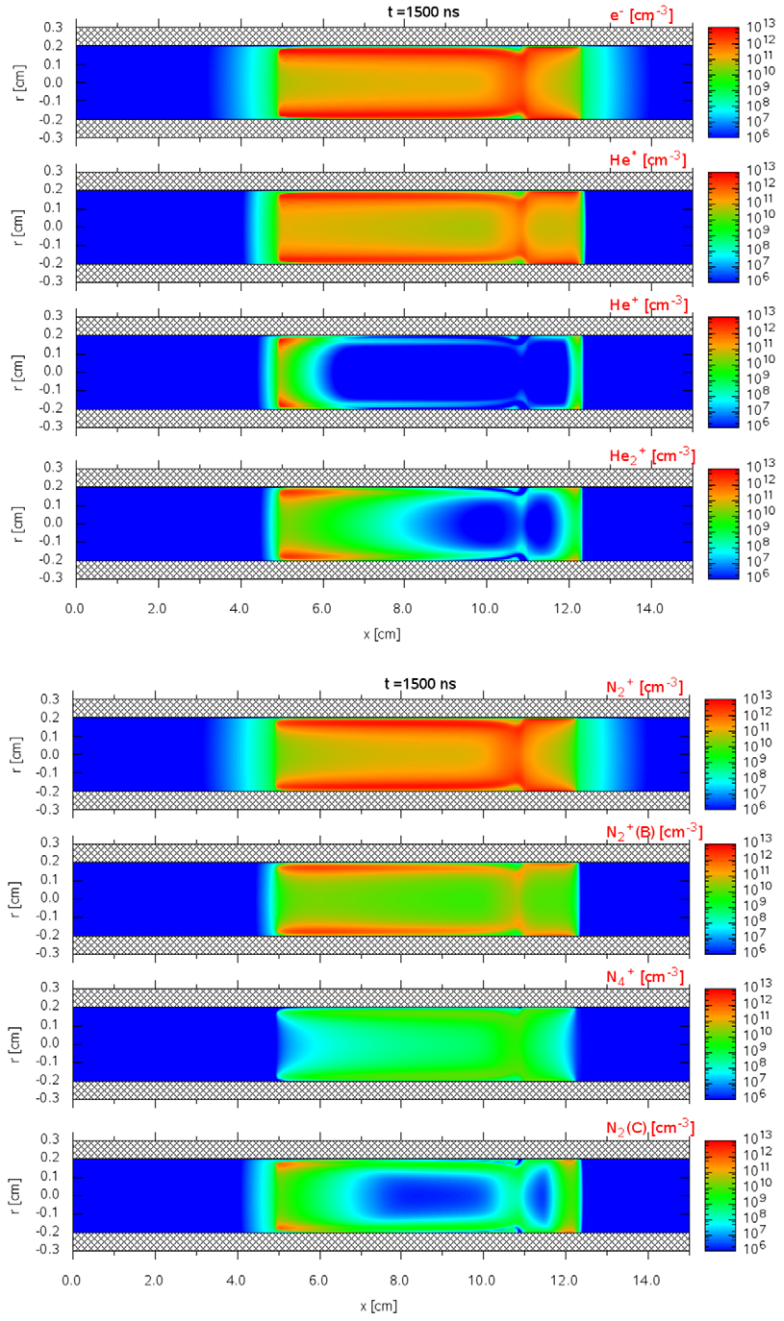

Figure 8. Cross-sectional views of all species at $t = 1500$ ns for the same conditions as figure 7.

decrease of ∼15% of the measured ignition time has been observed as the repetition rate increases by one order of magnitude (from 200 Hz to 2 kHz).

In simulations, the ignition time $\tau_{\text{igni}}^{\text{sim}}$ corresponds to the time when a peak electric field of about 8–10 $\text{kV} \cdot \text{cm}^{-1}$ is formed on the tube axis and starts to propagate towards the tube exit. In this work, as the geometry and the shape of the applied voltage are fixed to compare with experiments, a key parameter to vary the ignition time in the simulations is the initial preionization. We have checked that, as expected, photoionization has no influence on the ignition time. Then in table 3, we present the calculated ignition times $\tau_{\text{igni}}^{\text{sim}}$ for a preionization level n_{init} varying over eight orders of magnitude from $10^9\,\text{cm}^{-3}$, which has been used for 10 kHz pulsed discharges and gas flow velocities around $10^3\,\text{cm}\cdot\text{s}^{-1}$ (Naidis 2012b), to $10\,\text{cm}^{-3}$ which can be considered as the very low limit value of the 'natural' preionization (Pancheshnyi 2005). As expected, we note that both in experiments and in simulations, the ignition time decreases as the applied voltage increases. Table 3 shows that in simulations, the ignition time increases by 30% as the preionization decreases by eight orders of magnitude but remains slightly less than in experiments. However, as recently demonstrated in Robert *et al* (2015), the light emission from the ionization front, used to derive the experimental ignition time in table 3, is slightly delayed with respect to the electric field detected ahead of the ionization front. The typical time delay between the electric field rise and the light peak emission is of 500 ns (see figure 2, in Robert

Table 3. For 1000 ppm of N_2, influence of the preionization level n_{init} on the discharge ignition time in the simulations τ_{igni}^{sim}, and comparison with the measured ignition time τ_{igni}^{exp}.

Applied voltage (kV)	10	16
τ_{igni}^{exp} (ns)	1690	1240
τ_{igni}^{sim} (ns) for n_{init} =		
10 cm^{-3}	1500	1150
10^4 cm^{-3}	1400	1050
10^7 cm^{-3}	1100	900
10^9 cm^{-3}	1050	750

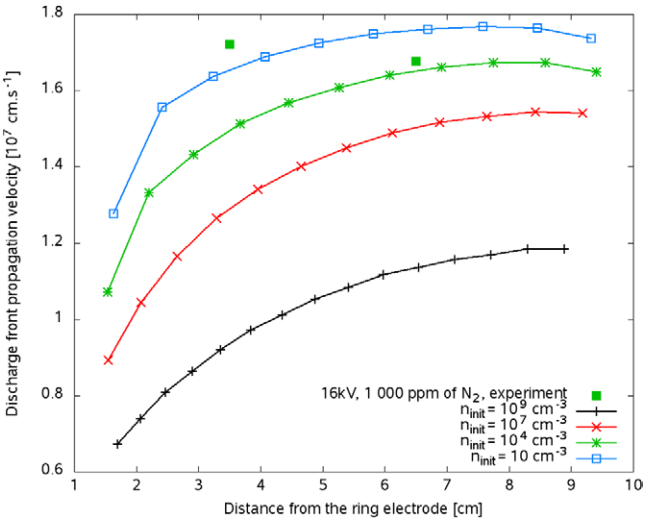

Figure 9. For an admixture of 1000 ppm of N_2, comparison of the experimental and numerical ionization front propagation velocities for an applied voltage of 16 kV. Simulations are carried out for different preionization levels n_{init} and a photoionization coefficient $A_{ph} = 10^{-2}$.

et al (2015)), so the delay between the time when the on-axis electric field amplitude is of 8–10 kV · cm^{-1} and the time of the emission peak is estimated to be of about 200–300 ns. This could explain the difference between the measured and computed ignition times of the discharge in table 3.

Figure 9 shows the influence of the preionization level n_{init} on the positive ionization front propagation velocity as a function of the distance from the ring electrode for an applied voltage of 16 kV and 1000 ppm of N_2. With the three optical fibers used in the experiments, two mean values of the measured ionization front propagation velocity between two consecutive fibers have been measured and are shown on figure 9 at 3.5 and 6.5 cm from the ring electrode. For all the cases presented on figure 9, we have checked in the simulations that the discharge propagates in the 10 cm long tube in less than 2 μs, the time of increase of the applied voltage. As a consequence, we note on figure 9 that for all cases the ionization front propagation velocity increases by 30–40% as the discharge propagates in the tube. However, it is interesting to note that the ionization front propagation velocity increases as the preionization level n_{init} decreases. Indeed, as the preionization level n_{init} decreases, the ignition time of the discharge slightly increases and then the discharge ignites at a slightly higher

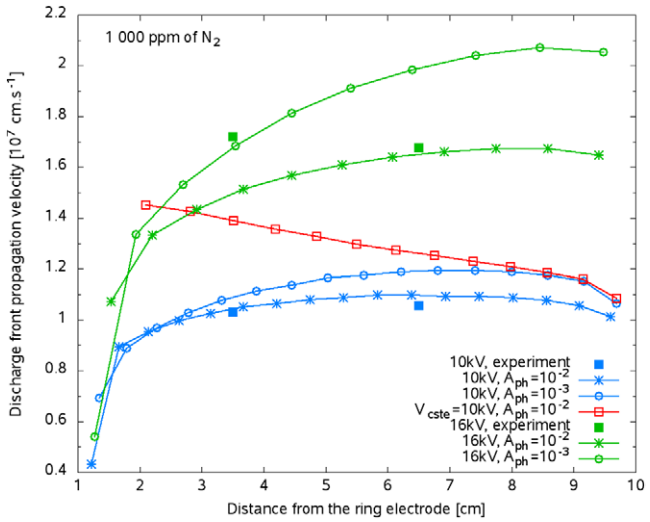

Figure 10. For an admixture of 1000 ppm of N_2, comparison of the experimental and numerical ionization front propagation velocities for applied voltages of 10 and 16 kV. Simulations are carried out with a preionization level $n_{init} = 10^4$ cm^{-3} and for two values of the photoionization coefficient $A_{ph} = 10X_{N_2} = 10^{-2}$ and $A_{ph} = X_{N_2} = 10^{-3}$.

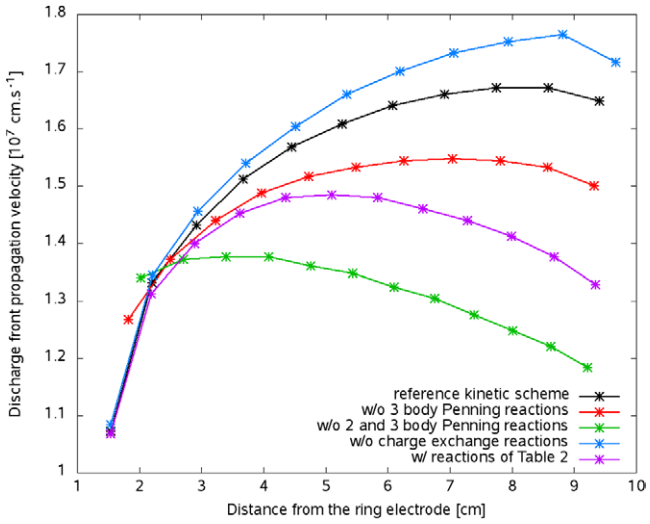

Figure 11. For an admixture of 1000 ppm of N_2 and an applied voltage of 16 kV, influence of the reactions considered in the kinetic scheme on the propagation velocity of the ionization front. Simulations are carried out with a preionization level $n_{init} = 10^4$ cm^{-3} and for a photoionization coefficient $A_{ph} = 10^{-2}$.

applied voltage which leads to a faster propagation. We note that the increase of velocity as the preionization decreases is faster as n_{init} decreases from 10^9 to 10^7 cm^{-3} than for values less than 10^7 cm^{-3}. It is interesting to note that a good agreement with experiments is obtained for a low preionization. Then, based on the comparison of experimental and simulated ignition times and ionization front propagation velocities, a low preionization level of $n_{init} = 10^4$ cm^{-3}, which is close to the 'natural' preionization, is used for all the simulation results presented in this work.

Figure 10 shows the comparison of the experimental and numerical ionization front propagation velocities as a function

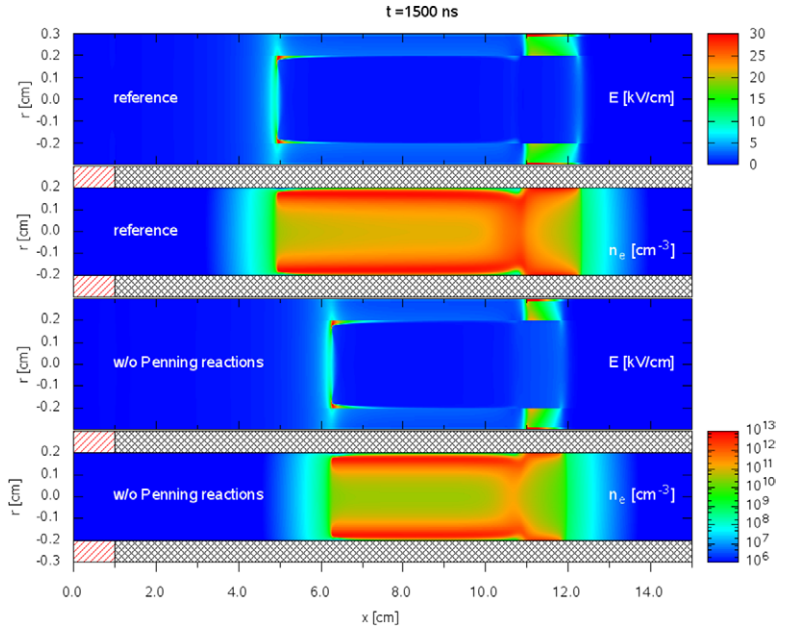

Figure 12. Cross-sectional views of the magnitude of the electric field and electron density at $t = 1500$ ns for an applied voltage of 16 kV, 1000 ppm of N_2, with a preionization level $n_{init} = 10^4$ cm^{-3} and for a photoionization coefficient $A_{ph} = 10^{-2}$ with the reference kinetic scheme and without two- and three-body Penning reactions.

of the distance from the ring electrode for applied voltages of 10 and 16 kV and for an admixture of 1000 ppm of N_2. Simulations are carried out for two values of the photoionization coefficient $A_{ph} = 10X_{N_2} = 10^{-2}$ and $A_{ph} = X_{N_2} = 10^{-3}$. It is interesting to note that a rather good agreement of the computed discharge velocities with the measured ones at 3.5 and 6.5 cm from the ring electrode is obtained for both applied voltages. As expected, we note that both in experiments and in simulations, the ionization front propagation velocities in the tube increase as the applied voltage increases. In experiments, for both voltages, the measured ionization front propagation velocities remain almost constant between 3.5 and 6.5 cm from the ring electrode. In simulations, for 16 kV and for both values of the photoionization coefficient, we have checked that the discharge propagates in the 10 cm long tube in less than 2 μs, the rise time of the applied voltage. Then in simulations, the ionization front propagation velocity increases slightly during its propagation until the end of the tube. Conversely, the discharge dynamics is slower for 10 kV and the peak voltage is reached when the ionization front is at 6 cm from the ring electrode. Therefore, on figure 10, we observe that the ionization front propagation velocity remains rather constant from 3 cm from the ring electrode until the end of the dielectric tube. Figure 10 shows that the value of the photoionization coefficient has only a small influence on the results and we observe only a slight increase of the discharge velocity as the photoionization coefficient $\xi = A_{ph}/X_{N_2}$ decreases by one order of magnitude, from 10 to 1. To show the influence of the shape of the applied voltage on the ionization front propagation velocity in the dielectric tube, we have also plotted on figure 10, the ionization front propagation velocity obtained in simulations for a constant applied voltage of 10 kV for $t \geqslant 0$s. We note that in this case, the ionization front propagation velocity decreases along the dielectric tube as already observed in Jánský and Bourdon (2011). The decrease is of about 20% at the end of the 10 cm tube. Then these results show clearly the influence of the value and the shape of the applied voltage on the ionization front propagation velocity in the dielectric tube.

4.2. Influence of the kinetic scheme on the discharge structure and dynamics for 1000 ppm of N_2

In this section, we study the influence of the kinetic scheme on the discharge structure and dynamics for the reference case with 1000 ppm of N_2. For an applied voltage of 16 kV, figure 11 shows the ionization front propagation velocity as a function of the distance from the ring electrode for different kinetic schemes. As mentioned in section 3, as a reference, we use the kinetic scheme given in table 1. To study the influence of Penning reactions on the discharge dynamics, we have redone the simulations without three-body Penning reactions (R10 and R21) and then two- and three-body Penning reactions (R9, R10, R20 and R21). In figure 11, we note that removing Penning reactions leads to a decrease of the ionization front velocity and to a change of its evolution along the tube length. It is important to note that for all the cases presented on figure 11, we have checked that the discharge propagates in the 10 cm long tube in less than 2 μs, the time of increase of the applied voltage. In the case without two- and three-body Penning reactions, the ionization front propagation velocity first increases up to 3.5 cm from the ring electrode and then decreases as it propagates further downstream. At 9 cm from the ring electrode (i.e. at 1 cm from the tube exit) the ionization front velocity is 28% less than in the reference case. Without only three-body Penning reactions, the ionization front velocity is only 9% less than in the reference case at 1 cm from the tube exit. Figure 12 compares the distributions of the electron density

and absolute values of the electric field at $t = 1500$ ns, for an applied voltage of 16 kV for the reference kinetic scheme of table 1 and without two- and three-body Penning reactions. We note that in both cases, the discharge structure is tubular but is slightly more homogeneous in the reference case. The results presented in figures 11 and 12 show that not only Penning reactions have an effect on the discharge dynamics, but also on its structure. It is important to underline that these reactions occur behind the ionization front. Indeed, for Penning reactions to occur, He^* excited atoms have first to be produced in the ionization front as shown in figure 8. However, as Penning reactions produce ions and electrons, when these reactions are excluded, the plasma column behind the ionization front becomes less conductive which leads to a slower propagation of the discharge in the tube. These results clearly show the importance of the plasma column on the discharge dynamics, in agreement with Shashurin *et al* (2009) and Shashurin *et al* (2012). Furthermore, as in this work a μs voltage pulse is used, the discharge dynamics may depend also on the recombination of ionic species in the plasma column. To illustrate this, first we have redone the simulations without two and three-body charge exchange reactions (R14, R15, R23 and R24). In this case, more He_2^+ ions remain in the plasma column and as the dissociative recombination rate coefficient of He_2^+ is less than those of N_2^+ and $N_2^+(B)$, the plasma column is more conductive without charge exchange reactions and we observe on figure 11 that the velocity of the ionization front is slightly higher than in the reference case. Second, on figure 11 we have added the results obtained with the reference kinetic scheme and the two reactions of table 2 related to the N_4^+ formation and discussed in section 3. In this case, we note that the ionization front velocity increases up to 5 cm from the high voltage ring electrode and then decreases and is 20% less than the reference one at 9 cm from the ring electrode (i.e. at 1 cm from the tube exit). It is interesting to note that in our conditions the three-body reaction R32 in table 2 is very efficient to convert N_2^+ in N_4^+ ions whereas the two-body reaction R33 which converts N_4^+ in N_2^+ ions has a negligible influence. Then, when the two reactions of table 2 are included, N_4^+ is the major ion in the plasma column. In table 1, we note that the dissociative recombination coefficient of N_4^+ ions (R30) is one order of magnitude higher then the one of N_2^+ (R22). Then, in the conditions studied in this work, this induces a decrease of the plasma column conductivity and then a slower discharge dynamics in comparison to the reference case and to experiments.

4.3. Comparison of the experimental and numerical results on the propagation velocity of the ionization front for various amounts of N_2

In this section, we study the influence of the amount of N_2 on the discharge structure and dynamics in the dielectric tube. In the conditions studied in this work, we have shown in the previous section that the kinetics in the plasma column has an impact on the discharge propagation. Based on the results obtained for 1000 ppm of N_2, we can assume that when the amount of N_2 is much less than 1000 ppm, Penning and charge transfer reactions which couple He and N_2 species will become inefficient and then the major ion in the plasma column will be He_2^+. As shown on figure 8, for 1000 ppm of N_2 the major ion is N_2^+ and for higher amounts of N_2, the major ion in the plasma column will be N_4^+. As all these ions have different recombination rate coefficients, we can expect different discharge dynamics in the tube as a function of the amount of N_2. However, it is important to note that when we vary the amount of N_2 in experiments and in simulations, we change not only the kinetics but also the photoionization source term, which may have an impact on the discharge structure and dynamics.

Table 4. Influence of the amount of N_2 admixture on the measured τ_{igni}^{exp} and computed τ_{igni}^{sim} ignition times of the discharge for an applied voltage of 16 kV with $n_{init} = 10^4$ cm^{-3}.

ppm of N_2	'0'	10	100	1000	5000	10 000
τ_{igni}^{exp} (ns)	1340	—	—	1240	1200	1340
τ_{igni}^{sim} (ns)	—	1150	1100	1050	1000	1050

First, in table 4 we compare the experimental and computed ignition times for various amounts of N_2 for an applied voltage of 16 kV and an initial preionization of $n_{init} = 10^4$ cm^{-3}.

Some experiments have been carried out without any N_2 admixture (and correspond to the '0' ppm of N_2 in table 4). However, even without admixture, there is a small amount of impurities in the helium gas. Therefore, it is more relevant to compare these experimental results with simulations carried out for 10 and 100 ppm of N_2. Then in table 4, experimental and computed ignition times for 1000, 5000 and 10 000 ppm of N_2 are compared. We have checked that, as already stated, photoionization has no influence on the ignition time. We note that the ignition time varies only slightly with the amount of N_2 admixture and that the computed ignition time is about 200 ns shorter than the measured one in all cases, as already observed in table 3 for 1000 ppm and commented in section 4.1. In section 4.2, for 1000 ppm of N_2, we have observed on figure 10 a rather good agreement of the computed ionization front propagation velocities with the measured ones for applied voltages of 10 and 16 kV. Then, figures 13 and 14 show the comparison of the experimental and numerical discharge velocities as a function of the distance from the ring electrode for 10, 100, 5000 and 10 000 ppm of N_2. On figure 13, we compare the experimental results for '0' ppm of N_2 with the computed ones for 10 and 100 ppm of N_2 for a photoionization coefficient $A_{ph} = 10X_{N_2}$. In simulations, we note that in the range 10 to 100 ppm, the amount of N_2 has only a small influence on the ionization front propagation velocity. Given the uncertainty on the amount of N_2 in the tube during experiments, we consider that the experiment-modeling agreement is rather good. On figure 14, we present experimental and numerical propagation velocities for 5000 and 10 000 ppm of N_2 and for two values of the photoionization coefficient $A_{ph} = 10X_{N_2}$ and $A_{ph} = X_{N_2}$. For 5000 ppm of N_2 on figure 14, a rather good agreement with experiments is obtained for 10 kV. For 16 kV, we observe that the simulated velocity increase close to the anode ring is smaller than in the measurements and then

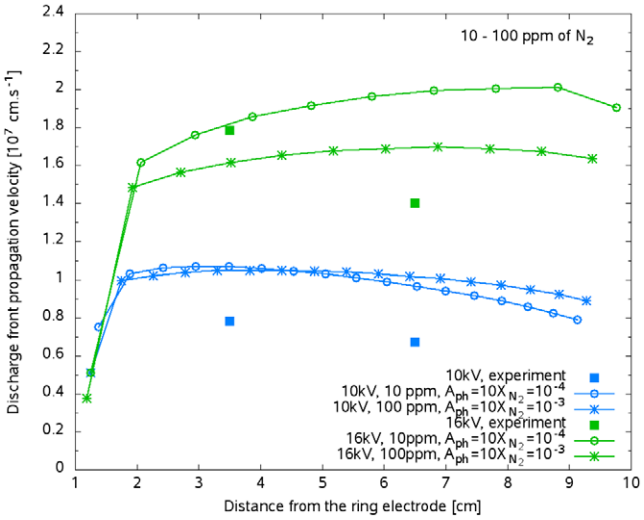

Figure 13. Comparison of the experimental discharge propagation velocities for '0' ppm of N_2 with the computed ones for 10–100 ppm of N_2 for applied voltages of 10 and 16 kV. Simulations are carried out with a preionization level $n_{\text{init}} = 10^4$ cm^{-3} and for a photoionization coefficient $A_{\text{ph}} = 10X_{N_2}$.

simulations understimate the velocity at 3.5 cm from the ring electrode. However, a rather good agreement is obtained at 6.5 cm from the ring electrode. We note that the influence of the photoionization coefficient is smaller for 5000 ppm than for 1000 ppm of N_2. For 10 000 ppm of N_2 on figure 14, for both voltages the simulations slightly underestimate the measured velocities. As already observed for 5000 ppm of N_2, we observe that the biggest discrepancy between experiments and simulations is for 16 kV and 3.5 cm from the ring electrode. It is interesting to note that the influence of the photoionization coefficient is small. However, we observe that the ionization front velocity increases as the photoionization coefficient increases by one order of magnitude, conversely to the case of 1000 ppm of N_2 on figure 10. Figure 15 shows the distributions of the electron density and absolute values of the electric field at $t = 1500$ ns, for an applied voltage of 16 kV for 5000 and 10 000 ppm of N_2 for $A_{\text{ph}} = 10X_{N_2}$. A tubular structure of the discharge is observed in both conditions, the discharge being slightly more homogeneous for 5000 ppm of N_2. Then, the results presented in this work show that the value of the ionization front propagation velocity depends on a complex coupling between the kinetics of the discharge, the photoionization and the 2D structure of the discharge in the tube, when the amount of N_2 is varied.

The comparison of experimental and numerical results confirms the significant influence of the amplitude of the applied voltage on the ionization front velocity in the discharge tube for all amounts of N_2. For the two studied applied voltages of 10 and 16 kV, in experiments and in simulations, we observe only a small influence of the amount of N_2 on the ionization front propagation velocity in the discharge tube. For 10 kV, both experimental and numerical results exhibit a small evolution of the ionization front propagation velocity along the tube length for all amounts of N_2. For 16 kV, simulations show for all amounts of N_2 first an increase of the ionization front propagation velocity as the discharge starts propagating in the

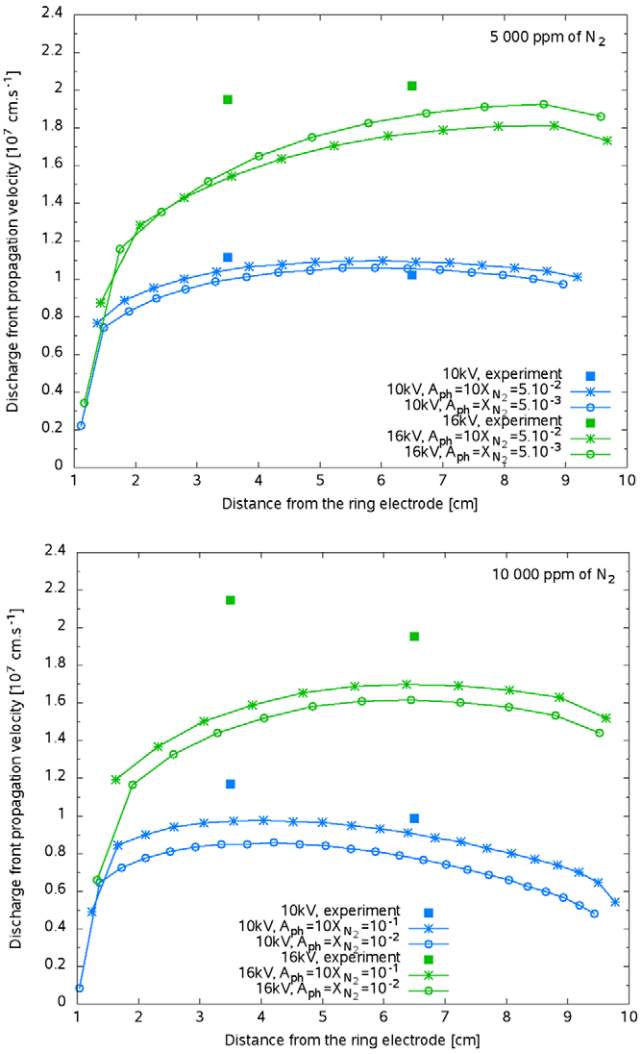

Figure 14. For admixtures of 5000 and 10 000 ppm of N_2, comparison of the experimental and numerical ionization front propagation velocities for applied voltages of 10 and 16 kV. Simulations are carried out with a preionization level $n_{\text{init}} = 10^4$ cm^{-3} and for two values of the photoionization coefficient A_{ph}.

tube which then tends to stabilize or slightly decrease along the tube. For 1000, 5000 and 10 000 ppm of N_2, the biggest discrepancy between experiments and simulations is at 3.5 cm from the anode ring for 16 kV. In experiments, as shown for example in figure 2 for 1000 ppm of N_2, we note that close to the anode ring, the velocity increase is rather rapid and then it appeared rather challenging to obtain a good experiment/modeling agreement in this discharge region at high voltage. Results obtained in this work show a much better experiment/modeling agreement for 16 kV downstream in the tube or for a lower voltage.

4.4. Comparison of the experimental and numerical time evolutions of the axial and radial electric fields

In experiments, as mentioned in section 2, the time evolutions of axial E_x and radial E_r components of the electric field have been measured by an electrooptic probe at different axial

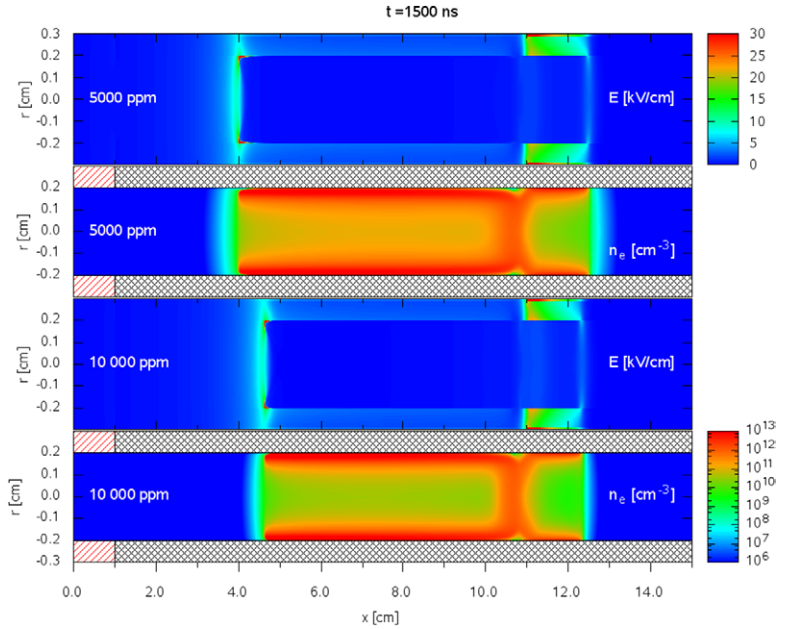

Figure 15. Cross-sectional views of the magnitude of the electric field and electron density at $t = 1500$ ns for 5000 and 10 000 ppm of N_2 for an applied voltage of 16 kV, with a preionization level $n_{init} = 10^4$ cm^{-3} and a photoionization coefficient $A_{ph} = 10X_{N_2}$.

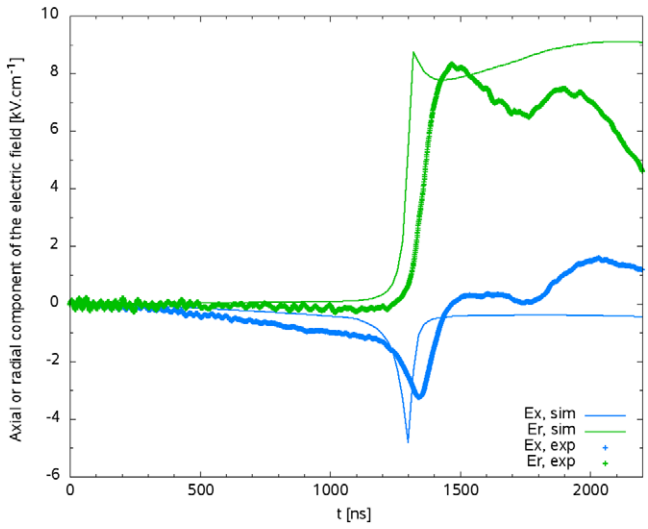

Figure 16. Time evolutions of the axial and radial components of the electric field measured by the probe and obtained in the simulations for 1000 ppm of N_2 and an applied voltage of 16 kV at a given axial position of 3 cm from the ring electrode and a radius of $r = 0.35$ cm.

and radial positions outside the dielectric tube. In this section, we compare these measurements with computed values of the electric field components at a given axial position of 3 cm from the ring electrode and a radius of $r = 0.35$ cm. For the simulation results presented in this section, the output timestep is of 20 ns. Figure 16 shows the time evolution of measured and computed E_x and E_r for 1000 ppm of N_2 and an applied voltage of 16 kV. A rather good agreement is observed both on the time evolutions and the values of the axial and radial components of the electric field. As measurements are done rather close to the dielectric tube, E_x at $r = 0.35$ cm is negative as is the axial electric field in the ionization front in the tube. The radial electric field E_r at $r = 0.35$ cm is positive and is due to the positive charge of the ionization front. On figure 16, we observe a first phase up to $t = 1200$ ns during which both axial and radial components have slow time evolutions and then a rapid variation of the E_x followed by the fast increase of E_r. Both axial and radial components reach peak values and it is interesting to note that peak absolute values for E_x are of about 3.5 to 5 kV $\cdot$ cm^{-1} and are higher and within 8.1 to 8.5 kV $\cdot$ cm^{-1} for E_r. We have checked in the simulations that the peaks of the electric field components correspond to the time of 1300 ns when the ionization front crosses the axial position of 3 cm from the ring electrode. After the peaks, the axial component decreases rapidly down to 0 whereas the radial component has a more complex time evolution. For plasma jet applications, it is of great interest to know the electric field in the dielectric tube and in the plasma plume at the tube exit. Based on the rather good agreement observed on figure 16 between experiments and simulations, we consider that a non-intrusive probe could be used outside of the tube and the plasma plume and that simulations could be used to infer the electric field in regions where it is difficult to measure it.

As an example, we present the numerical study of the influence of the amount of N_2 on the electric field in the ionization front in the tube. For an applied voltage of 16 kV, figure 17(a) shows the magnitude of the axial electric field on the symmetry axis as a function of the distance of the ionization front from the ring electrode for various amounts of N_2 ranging from 10 to 10 000 ppm. We note that the magnitude of the axial electric field on the symmetry axis depends weakly on the amount of N_2 and remains almost constant during the discharge propagation in the tube in the range of 8 to 10 kV $\cdot$ cm^{-1}. Figure 17(b) shows the magnitude of the off-axis peak electric field in the ionization front for the same conditions as figure 17(a). For all amounts of N_2 in the range of 10 to 10 000 ppm, the magnitude of the peak electric field in the ionization front remains almost constant all over the length of the discharge tube. For 16 kV

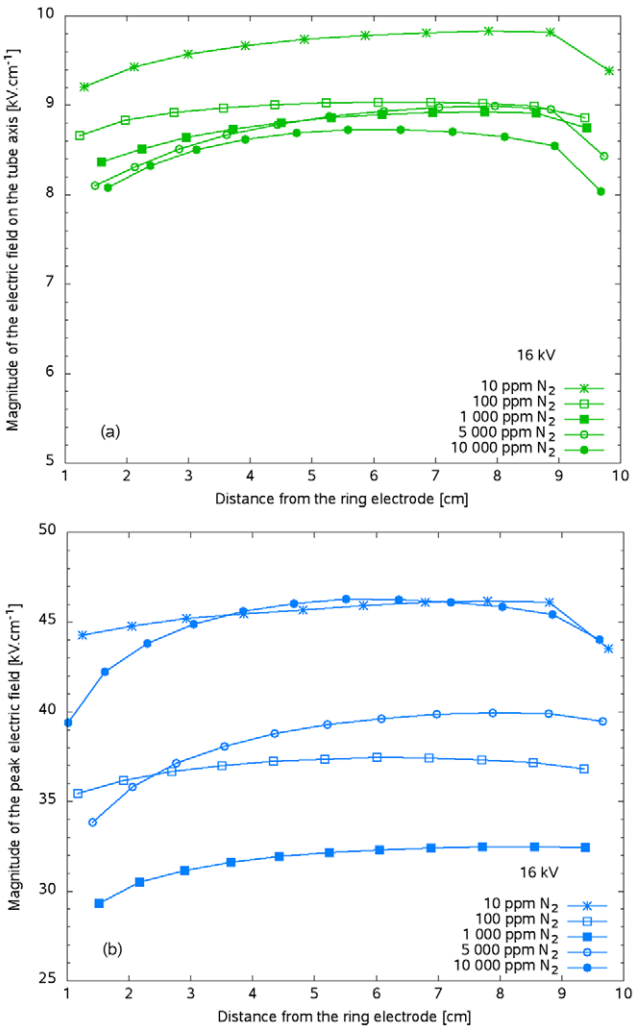

Figure 17. Magnitude of the electric field on the tube axis (a) and of the off axis peak electric field (b) as a function of the distance of the ionization front from the ring electrode for various amounts of N_2, for an applied voltage of 16 kV.

and 1000 ppm of N_2, the magnitude of the peak electric field in the ionization front is of about 30 $kV \cdot cm^{-1}$ and is larger than the electric field value on the discharge axis which corresponds to a tubular discharge structure as shown on figure 7. We observe this significant difference between the axial and off-axis magnitudes of the electric field for all amounts of N_2 shown on figure 17. It is interesting to note that the magnitude of the peak electric field in the ionization front depends on the amount of N_2. It is about 45 $kV \cdot cm^{-1}$ for 10 ppm of N_2 and then decreases rapidly as the quantity of N_2 increases and reaches a minimum of 30 $kV \cdot cm^{-1}$ for 1000 ppm of N_2. Then the magnitude of the peak electric field in the ionization front increases again more slowly as the amount of N_2 increases up to 45 $kV \cdot cm^{-1}$ for 10 000 ppm of N_2. In the simulations, we have checked that as the amount of N_2 increases up to 1000 ppm, the main ion rapidly changes from He_2^+ to N_2^+ and $N_2^+(B)$. Then for amounts of N_2 higher than 1000 ppm, a slow increase of $N_2(C)$ is observed as the amount of N_2 increases. It is interesting to note that these results are in good agreement with the changes in the emission spectra recorded experimentally and shown in figure 4. Indeed, as the amount of N_2 increases up to

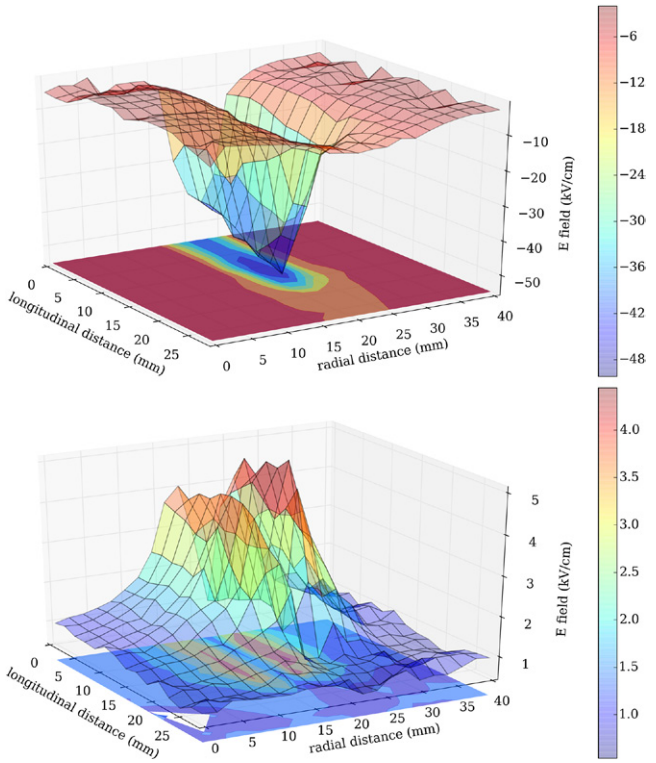

Figure 18. Top: 2D longitudinal peak electric field amplitude inside the plasma plume. Bottom: 2D radial peak electric field amplitude inside the plasma plume. The PG was used in basic set-up, 1000 sccm helium flow was flushed, a grounded target was set at 30 mm from PG capillary outlet (longitudinal distance origin 0 mm). The capillary axis corresponds to radial distance 20 mm.

1000 ppm, a rapid increase of the emission of N_2^{+*} is observed. Then for higher amounts of N_2, a slow increase of the emission of N_2^* is observed. The significant difference between the axial and off-axis magnitudes of the electric field, the variation of about 30% of the peak electric field values and the changes in the species produced by the discharge as a function of the amount of N_2 could be of key importance for interactions of the plasma plume with surfaces in biomedical applications.

Finally, we present measurements carried out with the sensor inside the visible plasma plume region and in its close vicinity in the basic PG set-up. The EF probe was moved all across the capillary to target gap, 30 mm on axis extension, and 20 mm left and right apart from the capillary axis. While the sensor spatial resolution is fixed by the crystal size (1 mm × 1.75 mm), a 1 mm increment step was used together with an averaging of EF signals over 512 voltage pulses to smooth the 2D maps and get an electric field characterization relevant for biomedical applications where thousands of PG pulses are used in experiments performed in the kHz regime during longer periods. While the EF probe is used here in an invasive way, it should be representative of situations where PG plasma plume is delivered over a target, and not in a so called free jet mode. Nevertheless, it must be pointed out that helium flow and mixture with ambient air is obviously disturbed due to the probe positioning inside the plasma plume so that complementary electric field measurements using optical diagnostics (Obradović *et al* 2008, Sretenović *et al* 2014, Goldberg *et al* 2015) would be valuable to confirm

the preliminary measurements shown in this work. Figure 18 reveals that the longitudinal electric field in the plume peaks along the capillary axis and is enhanced in the vicinity of the grounded target (longitudinal distance 30 mm). Longitudinal electric field peak amplitudes ranging from 30 to 50 kV·cm^{-1} are measured across the gap, where air admixture to the helium flow gradually occurs from the outlet of the capillary. The radial electric field amplitude are much lower reaching a maximum value of 4 kV·cm^{-1} and reveal a ring structure with a minimum on the plume axis and a peak amplitude 2 mm apart from this axis i.e. on the boundary of the visible plume. As the gas mixing downstream of the tube exit is not included in the model used in this work, a direct comparison with simulations is not intented. Nevertheless, it was shown by Breden *et al* (2012) and Naidis (2012a), that due to the gas mixing downstream of the tube exit, the annular discharge emerging from the tube transforms to a discharge more centered on the symmetry axis with maxima of electric field and charged and active species densities on the axis. Then, it is interesting to note that the peak electric field amplitudes, ranging from 30 to 50 kV·cm^{-1}, measured in the plume region on figure 18 are in good agreement with the peak electric fields calculated inside the capillary and shown on figure 17. These high values of electric field confirm that great care should be paid to the electric field topography during biomedical applications with plasma plumes.

5. Conclusions

The principal results and contributions, which follow from numerical and experimental studies presented in this paper on the influence of N_2 admixture on the dynamics of a μs helium plasma gun discharge in a 10 cm long tube, can be summarized as follows:

(i) We have put forward the importance to take into account a detailed kinetic scheme for the He–N_2 mixture in the simulations to obtain a good agreement with experiments on the ionization front propagation velocity. For the μs plasma gun discharge studied in this work, reactions occurring in the plasma column behind the ionization front, and in particular two- and three-body Penning reactions, are shown to play a significant role on the ionization front propagation in the dielectric tube. Finally, for atmospheric pressure plasma jets in He–N_2 mixtures, the kinetic scheme given in table 1 is recommended.

(ii) In experiments and simulations, the significant influence of the amplitude of the applied voltage on the value of the ionization front velocity in the tube is observed for all amounts of N_2. When the amount of N_2 is varied, simulations show that the ionization front propagation velocity which is a rather macroscopic quantity, depends on a complex coupling between the kinetics of the discharge, the photoionization and the 2D structure of the discharge in the tube. Then, for the conditions studied in this work with a plasma gun set-up adjusted for proper comparisons with simulations, the amount of N_2 is shown to have only a small influence on the ionization front velocity in experiments and simulations.

(iii) The good agreement obtained in this work between experiments and simulations on the time evolutions of the two components of the electric field, shows that a non-intrusive probe could be used outside of the tube and coupled to simulations to infer the electric field in regions where it is difficult to measure it. In the tube, simulations show that the magnitude of the axial electric field on the discharge axis depends weakly on the amount of N_2. The magnitude of the off-axis peak electric field decreases rapidly as the amount of N_2 increases up to 1000 ppm and then increases slowly for higher amounts of N_2. Simulations in the tube and first measurements in the plasma plume, put forward peak electric fields of the order of 45 kV·cm^{-1}. These high values could be of key importance for interactions of the plasma plume with surfaces in biomedical applications.

Acknowledgments

Simulations presented in this work have been performed thanks to the computational resources of the Mesocentre of Ecole Centrale Paris. Experiments have been supported by the ANR Blanc 'EXFIDIS' project (ANR-13-BS09-0014) and the APR Région Centre 'PLasmedNorm' project.

References

Algwari Q T and O'Connell D 2011 Electron dynamics and plasma jet formation in a helium atmospheric pressure dielectric barrier discharge jet *Appl. Phys. Lett.* **99** 121501

Boselli M, Colombo V, Gherardi M, Laurita R, Liguori A, Sanibondi P, Simoncelli E and Stancampiano A 2015 Characterization of a cold atmospheric pressure plasma jet device driven by nanosecond voltage pulses *IEEE Trans. Plasma Sci.* **43** 713–25

Bourdon A, Pasko V P, Liu N, Célestin S, Ségur P and Marode E 2007 Efficient models for photoionization produced by non-thermal gas discharges in air based on radiative transfer and the helmholtz equations *Plasma Sources Sci. Technol.* **16** 656–78

Breden D, Miki K and Raja L L 2012 Self-consistent two-dimensional modeling of cold atmospheric-pressure plasma jets/bullets *Plasma Sources Sci. Technol.* **21** 034011

Darny T, Robert E, Dozias S and Pouvesle J 2014 Selective reactive species production in a μs helium plasma gun discharge *Proc. 5th Int. Conf. on Plasma Medicine (Nara, Japan)*

Ellis H W, Pai R Y, McDaniel E W, Mason E A and Viehland L A 1976 Transport properties of gaseous ions over a wide energy range *At. Data Nucl. Data Tables* **17** 177

Fridman G, Friedman G, Gutsol A, Shekhter A B, Vasilets V N and Fridman A 2008 Applied plasma medicine *Plasma Process. Polym.* **5** 503–33

Gazeli K, Doanh L, Clement F, Svarnas P, Ricard A, Duday D and Belmonte T 2012 Spectroscopic study of atmospheric pressure plasma jets generated with DBD in gas mixtures of He-Ar-N_2 *Proc. ESCAMPIG XXI (Viana do Castelo, Portugal)*

Goldberg B M, Böhm P S, Czarnetzki U, Adamovich I V and Lempert W R 2015 Electric field vector measurements in a surface ionization wave discharge *Plasma Sources Sci. Technol.* **24** 055017

Hagelaar G J M and Pitchford L C 2005 Solving the Boltzmann equation to obtain electron transport coefficients and rate coefficients for fluid models *Plasma Sources Sci. Technol.* **14** 722–33

Hairer E and Wanner G 1996 *Solving Ordinary Differential Equations* II 2nd edn (Berlin: Springer)
Hübner S, Sousa J S, Puech V, Kroesen G M W and Sadeghi N 2014 Electron properties in an atmospheric helium plasma jet determined by Thomson scattering *J. Phys. D: Appl. Phys.* **47** 432001
HYPRE 2007 HYPRE: a library of high performance preconditioners https://computation.llnl.gov/project/linear_solvers/
Iseni S, Zhang S, van Gessel F, Hofmann S, van Ham B, Reuter S, Weltmann K-D and Bruggeman P 2014 Nitric oxide density distributions in the effluent of an RF argon APPJ: effect of gas flow rate and substrate *New J. Phys.* **16** 123011
IST-Lisbon database (retrieved on March 2014) www.lxcat.net
Jánský J and Bourdon A 2011 Simulation of helium discharge ignition and dynamics in thin tubes at atmospheric pressure *Appl. Phys. Lett.* **99** 161504
Jánský J and Bourdon A 2014 Simulation of two counter-propagating helium discharges at atmospheric pressure *Plasma Sources Sci. Technol.* **23** 025001
Kossyi I A, Kostinsky A Y, Matveyev A A and Silakov V P 1992 Kinetic scheme of the non-equilibrium discharge in nitrogen-oxygen mixtures *Plasma Sources Sci. Technol.* **1** 207–20
Lazarou C, Koukounis D, Chiper A S, Costin C, Topala I and Georghiou G E 2015 Numerical modeling of the effect of the level of nitrogen impurities in a helium parallel plate dielectric barrier discharge *Plasma Sources Sci. Technol.* **24** 035012
Lieberman M A 2015 Analytical model of atmospheric pressure, helium/trace gas radio-frequency capacitive Penning discharges *Plasma Sources Sci. Technol.* **24** 025009
Liu N, Célestin S, Bourdon A, Pasko V P, Ségur P and Marode E 2007 Application of photoionization models based on radiative transfer and the Helmholtz equations to studies of streamers in weak electric fields *Appl. Phys. Lett.* **91** 211501
Lu X, Laroussi M and Puech V 2012 On atmospheric-pressure non-equilibrium plasma jets and plasma bullets *Plasma Sources Sci. Technol.* **21** 034005
Martens T, Bogaerts A, Brok W J M and Dijk J V 2008 The dominant role of impurities in the composition of high pressure noble gas plasmas *Appl. Phys. Lett.* **92** 041504
Murakami T, Niemi K, Gans T, O'Connell D and Graham W G 2013 Chemical kinetics and reactive species in atmospheric pressure helium–oxygen plasmas with humid-air impurities *Plasma Sources Sci. Technol.* **22** 015003
Naidis G 2011a Simulation of streamers propagating along helium jets in ambient air: polarity-induced effects *Appl. Phys. Lett.* **98** 141501
Naidis G V 2010 Modelling of streamer propagation in atmospheric-pressure helium plasma jets *J. Phys. D: Appl. Phys.* **43** 402001
Naidis G V 2011b Modelling of plasma bullet propagation along a helium jet in ambient air *J. Phys. D: Appl. Phys.* **44** 215203
Naidis G V 2012a Modeling of helium plasma jets emerged into ambient air: influence of applied voltage, jet radius, and helium flow velocity on plasma jet characteristics *J. Appl. Phys.* **112** 103304
Naidis G V 2012b Simulation of interaction between two counter-propagating streamers *Plasma Sources Sci. Technol.* **21** 034003
Obradović B M, Ivković S S and Kuraica M M 2008 Spectroscopic measurement of electric field in dielectric barrier discharge in helium *Appl. Phys. Lett.* **92** 191501
Pancheshnyi S 2005 Role of electronegative gas admixtures in streamer start, propagation and branching phenomena *Plasma Sources Sci. Technol.* **14** 645–53
Pechereau F 2013 Numerical simulation of the interaction of a plasma discharge at atmospheric pressure with dielectric surfaces *PhD Thesis* Ecole Centrale Paris
Pechereau F, Jánský J and Bourdon A 2012 Simulation of the reignition of a discharge behind a dielectric layer in air at atmospheric pressure *Plasma Sources Sci. Technol.* **21** 055011
Petrov G M *et al* 2000 Numerical modeling of a He-N_2 capillary surface wave discharge at atmospheric pressure *Plasma Chem. Plasma Process.* **20** 183–207
Pouvesle J M, Bouchoule A and Stevefelt J 1982 Modeling of the charge transfer afterglow excited by intense electrical discharges in high pressure helium nitrogen mixtures *J. Chem. Phys.* **77** 817–25
Reuter S, Tresp H, Wende K, Hammer M, Winter J, Masur K, Schmidt-Bleker A and Weltmann K 2012 From RONS to ROS: tailoring plasma jet treatment of skin cells *IEEE Trans. Plasma Sci.* **40** 2986–93
Robert E, Sarron V, Riès D, Dozias S, Vandamme M and Pouvesle J-M 2012 Characterization of pulsed atmospheric-pressure plasma streams (PAPS) generated by a plasma gun *Plasma Sources Sci. Technol.* **21** 034017
Robert E *et al* 2013 Perspectives of endoscopic plasma applications *Clin. Plasma Med.* **1** 8–16
Robert E, Darny T Iséni S and Pouvesle J-M 2015 New insights on the propagation of pulsed atmospheric plasma streams: from single jet to multi jet arrays *Phys. Plasmas* **22** 122007
Sakiyama Y and Graves D 2006 Finite element analysis of an atmospheric pressure rf-excited plasma needle *J. Phys. D: Appl. Phys.* **39** 3451
Shashurin A, Shneider M N, Dogariu A, Miles R B and Keidar M 2009 Temporal behavior of cold atmospheric plasma jet *Appl. Phys. Lett.* **94** 231504
Shashurin A, Shneider M N and Keidar M 2012 Measurements of streamer head potential and conductivity of streamer column in cold nonequilibrium atmospheric plasmas *Plasma Sources Sci. Technol.* **21** 034006
Sommerer T J and Kushner M J 1992 Numerical investigation of the kinetics and chemistry of rf glow discharge plasmas sustained in He, N_2, O_2, He/N_2/O_2, He/CF_4/O_2, and SiH_4/NH_3 using a monte carlo-fluid hybrid model *J. Appl. Phys.* **71** 1654–73
Sretenović G B, Krstić I B, Kovačević V V, Obradović B M and Kuraica M M 2014 Spatio-temporally resolved electric field measurements in helium plasma jet *J. Phys. D: Appl. Phys.* **47** 102001
van Gessel B, Brandenburg R and Bruggeman P 2013 Electron properties and air mixing in radio frequency driven argon plasma jets at atmospheric pressure *Appl. Phys. Lett.* **103** 064103
von Woedtke T, Reuter S, Masur K and Weltmann K-D 2013 Plasmas for medicine *Phys. Rep.* **530** 291–320
Winter J, Brandenburg R and Weltmann K-D 2015a Atmospheric pressure plasma jets: an overview of devices and new directions *Plasma Sources Sci. Technol.* **24** 064001
Winter J, Sousa J S, Sadeghi N, Schmidt-Bleker A, Reuter S and Puech V 2015b The spatio-temporal distribution of he (2^3S_1) metastable atoms in a MHz-driven helium plasma jet is influenced by the oxygen/nitrogen ratio of the surrounding atmosphere *Plasma Sources Sci. Technol.* **24** 025015
Xiong Z and Kushner M 2012 Atmospheric pressure ionization waves propagating through a flexible high aspect ratio capillary channel and impinging upon a target *Plasma Sources Sci. Technol.* **21** 034001
Xiong Z, Robert E, Sarron V, Pouvesle J-M and Kushner M J 2012 Dynamics of ionization wave splitting and merging of atmospheric-pressure plasmas in branched dielectric tubes and channels *J. Phys. D: Appl. Phys.* **45** 275201
Xiong Z, Robert E, Sarron V, Pouvesle J-M and Kushner M J 2013 Atmospheric-pressure plasma transfer across dielectric channels and tubes *J. Phys. D: Appl. Phys.* **46** 155203
Zhang P and Kortshagen U 2006 2D numerical study of atmospheric pressure glows in helium with impurities *J. Phys. D: Appl. Phys.* **39** 153
Zhang Q, Zhuang J, von Woedtke T, Kolb J F, Zhang J, Fang J and Weltmann K-D 2014 Synergistic antibacterial effects of treatments with low temperature plasma jet and pulsed electric fields *Appl. Phys. Lett.* **105** 104103